




# An effective equation for quasi-one-dimensional funnel-shaped Bose–Einstein condensates with embedded vorticity

Mateus C. P. dos Santos<sup>1,a</sup>, Wesley B. Cardoso<sup>1,b</sup> , and Boris A. Malomed<sup>2,3,c</sup>

<sup>1</sup> Instituto de Física, Universidade Federal de Goiás, 74.690-970 Goiânia, Goiás, Brazil

<sup>2</sup> Department of Physical Electronics, School of Electrical Engineering, Faculty of Engineering, Tel Aviv University, Tel Aviv 69978, Israel

<sup>3</sup> Instituto de Alta Investigación, Universidad de Tarapacá, Casilla 7D, Arica, Chile

Received 10 July 2021 / Accepted 19 November 2021 / Published online 7 December 2021

© The Author(s), under exclusive licence to EDP Sciences, Springer-Verlag GmbH Germany, part of Springer Nature 2021

**Abstract** On the basis of a recently introduced model for the Bose–Einstein condensate (BEC) trapped in the 2D “funnel” potential,  $\sim -r^{-1}$ , we develop analysis for vortex modes, which are confined in the transverse direction by the self-attraction, or by the trapping potential, in the case of self-repulsion. Linear 3D wave functions are found exactly for eigenstates with an orbital momentum. In the case of self-repulsion, 3D wave functions are obtained by means of the Thomas–Fermi approximation. Then, with the help of the variational method, the underlying Gross–Pitaevskii equation is reduced to a 1D nonpolynomial Schrödinger equation (NPSE) for modes with zero or nonzero embedded vorticity, which are tightly confined by the funnel potential in the transverse plane. Numerical results demonstrate high accuracy of the NPSE reduction for both signs of the nonlinearity. The analysis is performed for stationary modes and for traveling ones colliding with a potential barrier. By means of simulations of NPSE with the self-attraction, collisions between solitons are studied too, demonstrating elastic and inelastic outcomes, depending on the impact velocity and underlying vorticity. A boundary of the stability of 3D vortices with winding number  $S = 1$  against spontaneous splitting in two fragments is identified in the case of the self-attraction, all vortices with  $S \geq 2$  being unstable.

## 1 Introduction

The Bose–Einstein condensation (BEC) occurs when a gas of bosons is cooled to ultra-low temperatures which allow a large fraction of bosons to occupy the lowest quantum state [1–3]. Atomic BECs were first observed in vapors of  $^{87}\text{Rb}$  [4],  $^{23}\text{Na}$  [5], and  $^7\text{Li}$  [6] confined by trapping fields and cooled down to temperatures  $\sim 100$  nK. Then, the production of matter-wave dark and bright solitons was reported, respectively, in condensates of  $^{87}\text{Rb}$  [7] and  $^7\text{Li}$  [8,9] atoms (and later in the condensate of  $^{85}\text{Rb}$  [10]). The generation of solitons was facilitated by the use of phase engineering [11] and magnetically controlled Feshbach resonance [9]. Matter-wave solitons offer potential applications, such as quantum information processing, atomic lasers and high-precision atomic interferometers [12–15]. Recently, the creation of robust breathers (higher order solitons featuring internal oscillations) has been reported too [16,17]. Related results are the predic-

tion [18,19] and experimental demonstration [20–23] of “quantum droplets”, i.e., self-trapped three- and quasi-two-dimensional (3D and quasi-2D) states stabilized by quantum fluctuations around mean-field configurations, see also recent reviews [24,25].

In the mean-field approximation, a weakly interacting bosonic gas is accurately modeled by the Gross–Pitaevskii equation (GPE) [1–3]. It adequately captures basic properties exhibited by superfluid systems, such as the propagation of collective excitations and interference patterns originating from the phase of the order parameter. The analysis may be further simplified by reducing the 3D GPE to the quasi-1D approximation for BEC freely evolving in the longitudinal direction, while being tightly confined in the transverse plane by a harmonic potential with trapping frequency  $\omega_{\perp}$  [26–32] (see also Refs. [33–38] dealing with related models). In particular, the resulting 1D and 2D (in the case when the tight transverse confinement is applied in one direction) nonpolynomial nonlinear Schrödinger equations (NPSEs), derived by Salasnich et al. [28] and Muñoz-Mateo and Delgado [39], provide very accurate approximations for the mean-field dynamics of BEC with attractive and repulsive interatomic interactions,

<sup>a</sup> e-mail: [mateuscalixtopereira@gmail.com](mailto:mateuscalixtopereira@gmail.com)

<sup>b</sup> e-mail: [wesleybcardoso@ufg.br](mailto:wesleybcardoso@ufg.br) (corresponding author)

<sup>c</sup> e-mail: [malomed@tauex.tau.ac.il](mailto:malomed@tauex.tau.ac.il)

respectively. In this context, many BEC configurations with the reduced dimensionality have been studied by means of the variational approximation [40–49] and in the adiabatic limit [50–60].

A change in the transverse-confinement pattern affects the resulting nonlinearity in the resulting quasi-1D (or quasi-2D) equation. In particular, a quasi-1D approximation was recently developed for the ground states of BEC transversely trapped by a singular but physically relevant *funnel potential*  $\sim -1/r$  (where  $r$  is the radial coordinate in the transverse plane) [61]. A physical realization of this potential can be provided by atoms with a permanent magnetic moment, pulled to the central electric current (e.g., electron beam) flowing along the  $z$  axis [61].

In the present work, we address vortex modes in BEC loaded in the funnel potential. The setting is similar to that introduced in Ref. [61] where, however, vortices were not considered. The results obtained from the respective quasi-1D effective equation are compared to those produced by a numerical solution of the full 3D GPE, for both repulsive and attractive signs of the nonlinearity, i.e.,  $g > 0$  and  $g < 0$  in Eq. (1), see below. In particular, we consider collisions of the modes considered in this work with a Gaussian barrier, and head-on collisions between ground and vortex states.

The rest of the paper is organized as follows. In the next section, we derive the effective NPSE produced by the 3D→1D reduction. The validation of the effective model by comparison with numerical simulations of the full 3D GPE are displayed in Sect. 3, where we report results for both ground and vortex states, as well as for dynamical situations. The paper is concluded Sect. 4.

## 2 The derivation of the effective nonpolynomial Schrödinger equation

### 2.1 Three-dimensional approximations

Our starting point is the 3D GPE written in the scaled form,

$$i\frac{\partial\psi}{\partial t} = -\frac{1}{2}\nabla^2\psi + V(r, z)\psi + 2\pi g|\psi|^2\psi, \quad (1)$$

where  $\psi = \psi(r, \theta, z, t)$  is the macroscopic wave function, normalized to unity:

$$\int_0^\infty r dr \int_0^{2\pi} d\theta \int_{-\infty}^{+\infty} |\psi(r, \theta, z)|^2 dz = 1, \quad (2)$$

where  $(r, \theta, z)$  is the set of cylindrical coordinates, and  $V = V(r, z)$  is an external axisymmetric potential produced by a magneto-optical trap. The scaled variables are related to their counterparts with tildes, measured in physical units:

$$t \equiv \omega_\perp \tilde{t}, \quad (r, z) \equiv (\tilde{r}, \tilde{z})/a_\perp, \quad \psi \equiv \tilde{\psi} a_\perp^{3/2}, \quad (3)$$

where the characteristic length,  $a_\perp = \sqrt{\hbar/(m\omega_\perp)}$ , is determined by the above-mentioned trapping frequency,  $\omega_\perp$ , and the self-interaction coefficient in Eq. (1) is  $g = 2a_s/a_\perp$ , with scattering length  $a_s$  of atomic collisions.

GPE (1) conserves the total norm, which is set to be 1 in Eq. (2), angular momentum,

$$M = -i \int_0^\infty r dr \int_0^{2\pi} d\theta \int_{-\infty}^{+\infty} dz \frac{\partial\psi}{\partial\theta} \psi^*, \quad (4)$$

where  $*$  stands for the complex conjugate, and Hamiltonian

$$H = \int_0^\infty r dr \int_0^{2\pi} d\theta \int_{-\infty}^{+\infty} dz \mathcal{H} \quad (5)$$

with density

$$\mathcal{H} = \frac{1}{2} \left( \left| \frac{\partial\psi}{\partial r} \right|^2 + r^{-2} \left| \frac{\partial\psi}{\partial\theta} \right|^2 + \left| \frac{\partial\psi}{\partial z} \right|^2 \right) + V(r, z)|\psi|^2 + \pi g|\psi|^4. \quad (6)$$

Vortex states with integer winding number  $S \geq 0$  are looked for by substituting

$$\psi = \exp(iS\theta)\phi(r, z, t) \quad (7)$$

in Eq. (1), which leads to the equation in the  $(r, z)$  plane,

$$i\frac{\partial\phi}{\partial t} = -\frac{1}{2} \left( \frac{\partial}{\partial r^2} + \frac{1}{r} \frac{\partial}{\partial r} + \frac{\partial^2}{\partial z^2} \right) \phi + W(r)\phi + \frac{S^2}{2r^2}\phi + V(z)\phi + 2\pi g|\phi|^2\phi, \quad (8)$$

where we define the above-mentioned funnel potential as per Ref. [61],

$$W(r) \equiv -\frac{\varepsilon^3}{2r}, \quad (9)$$

with  $\varepsilon > 0$  (by means of rescaling, we fix  $\varepsilon = 1$ ), and  $V(z)$  is a generic axial potential. In this work, we consider a harmonic-oscillator trap acting in the  $z$  direction, i.e.,

$$V(z) = (\lambda^2/2) z^2, \quad (10)$$

with  $\lambda \ll 1$ . The combination of the attractive term (9) and confining one (10) implies a 3D cigar-shaped potential configuration stretched in the  $z$  direction.

Spatially localized stationary solutions to Eq. (8) with chemical potential  $\mu$  are looked for as

$$\phi = \exp(-i\mu t)u(r, z), \quad (11)$$

with real function  $u$  satisfying equation

$$\begin{aligned} \mu u = & -\frac{1}{2} \left( \frac{\partial}{\partial r^2} + \frac{1}{r} \frac{\partial}{\partial r} + \frac{\partial^2}{\partial z^2} \right) u \\ & + \left( -\frac{1}{2r} + \frac{S^2}{2r^2} + \frac{\lambda^2}{2} z^2 \right) u + 2\pi g u^3 \end{aligned} \quad (12)$$

(recall  $\varepsilon = 1$  is set in Eq. (9)). Note that, for stationary states given by Eq. (11), Eqs. (4) and (7), along with normalization condition (2), yield a simple result,  $M = S$ .

The linearized version of Eq. (12) admits an exact *yrast* solution (i.e., the lowest energy eigenstate for given vorticity  $S$  [62,63]):

$$u = u_0 r^S \exp \left( -\frac{1}{1+2S} r - \frac{\lambda}{2} z^2 \right), \quad (13)$$

$$\mu = -\frac{1}{2(1+2S)^2} + \frac{\lambda}{2}, \quad (14)$$

with arbitrary constant  $u_0$ . In the case of  $S = 0$ , this solution is the system’s ground state. For  $S \geq 1$ , the expansion of the *yrast* eigenfunction at  $r \rightarrow 0$ , in the form of

$$u = u_0 \exp \left( -\frac{\lambda}{2} z^2 \right) \left( r^S - \frac{1}{1+2S} r^{S+1} \right) + O(r^{S+2}), \quad (15)$$

is not affected by the nonlinearity in Eq. (11), hence it is a universal asymptotic form valid at  $r \rightarrow 0$ . Note that the chemical potential, corresponding to the bound state (13), as given by Eq. (14), may be both negative and positive, due to the contribution from the trapping potential (10).

Further, in the case of the self-repulsion, i.e.,  $g > 0$  in Eq. (12), 3D localized states (corresponding to  $\mu < 0$ ) can be constructed in the framework of the Thomas–Fermi (TF) approximation, which neglects derivatives in Eq. (12):

$$u_{\text{TF}}^2 = \frac{1}{4\pi g} \left[ \frac{1}{4S^2} + 2\mu - S^2 \left( \frac{1}{r} - \frac{1}{2S^2} \right)^2 - \lambda^2 z^2 \right], \quad (16)$$

$$\begin{aligned} & \text{at } S^2 \left( \frac{1}{r} - \frac{1}{2S^2} \right)^2 + \lambda^2 z^2 \leq \frac{1}{4S^2} + 2\mu; \\ & u_{\text{TF}}^2 = 0, \\ & \text{at } S^2 \left( \frac{1}{r} - \frac{1}{2S^2} \right)^2 + \lambda^2 z^2 \geq \frac{1}{4S^2} + 2\mu, \end{aligned} \quad (17)$$

Note that this solution exists in the band of values of the chemical potential

$$0 < -\mu < -\mu_{\text{cutoff}} \equiv 1/(8S^2). \quad (18)$$

Comparison of Eqs. (18) and (14) suggests that the TF approximation is accurate enough for small  $\lambda$  and relatively large values of vorticity  $S$ . It is seen that it produces the solution in area (17), which is an ellipse in the plane of  $(r^{-1}, z)$ , or an annulus in the plane of  $(r, z)$ , with the radial and axial coordinates varying in intervals

$$\frac{2S^2}{1 + \sqrt{1 + 8\mu S^2}} < r < \frac{2S^2}{1 - \sqrt{1 + 8\mu S^2}}, \quad (19)$$

$$|z| < \lambda^{-1} \sqrt{\frac{1}{4S^2} + 2\mu}. \quad (20)$$

The TF approximation is irrelevant for the ground states with  $S = 0$  (therefore it was not elaborated in Ref. [61]), while the fact that this approach may be, generally, relevant for modes of the vortex type is known in other contexts [64,65].

Lastly, normalization condition (2), if applied to the TF solution (16), can be written explicitly in the limit when  $\mu$  is close to the cutoff given by Eq. (18):

$$\mu - \mu_{\text{cutoff}} = \sqrt{\frac{g\lambda}{8\pi S^5}}. \quad (21)$$

In fact, Eq. (21) determines relation  $\mu(g)$  corresponding to the unitary normalization, being valid, in accordance with what is said above, for relatively large  $S$  and small  $\lambda$ .

### 2.2 The one-dimensional equation

To implement the 3D  $\rightarrow$  1D reduction, we adopt an *ansatz* which assumes factorization of the wave function, and the decay exponential profile in the radial direction, with pre-exponential factor  $r^S$  representing the standard form of the vortex wave functions at  $r \rightarrow 0$ :

$$\psi(r, \theta, z, t) = \frac{r^S \exp \left[ -\frac{r}{2\sigma(z, t)^2} + iS\theta \right] f(z, t)}{\sqrt{2\pi\Gamma(2+2S)[\sigma(z, t)]^{4+4S}}}, \quad (22)$$

Here,  $\Gamma$  is the Euler’s Gamma function, while  $\sigma = \sigma(z, t)$  and  $f(z, t)$  are the transverse width and axial wave function, respectively. The structure of the *ansatz* provides the reduction of the 3D density to its effective 1D counterpart,

$$\int_0^\infty \int_0^{2\pi} |\psi|^2 r dr d\theta = |f(z)|^2. \quad (23)$$

The substitution of *ansatz* (22) in the Lagrangian density that generates the 3D GPE (1),  $\mathcal{L} = i\psi^* \partial\psi/\partial t - \mathcal{H}$  (see Eq. (6)), and integration with respect to radial

coordinate  $r$  yields an effective 1D Lagrangian density,

$$\begin{aligned} \mathcal{L}_{1D} = & \frac{i}{2} \left( f^* \frac{\partial f}{\partial t} - f \frac{\partial f^*}{\partial t} \right) - \frac{1}{2} \left| \frac{\partial f}{\partial z} \right|^2 \\ & - \frac{[(2 + 4S)\sigma^2 V(z) - 1]}{(2 + 4S)\sigma^2} |f|^2 - \frac{1}{8\sigma^4} |f|^2 \\ & - \frac{g\Gamma\left(\frac{3}{2} + 2S\right)}{\sqrt{\pi}(4 + 8S)\Gamma(2 + 2S)\sigma^4} |f|^4. \end{aligned} \tag{24}$$

From this density, one can derive the following system of coupled 1D Euler–Lagrange equations:

$$\begin{aligned} i \frac{\partial f}{\partial t} = & -\frac{1}{2} \frac{\partial^2 f}{\partial z^2} + V(z)f + \frac{[2S - 4\sigma^2 + 1]}{(16S + 8)\sigma^4} f \\ & + \frac{\Gamma\left(\frac{3}{2} + 2S\right) g |f|^2}{\sqrt{\pi}\Gamma(2 + 2S)(2 + 4S)\sigma^4} f, \end{aligned} \tag{25}$$

$$\sigma^2 = \frac{g|f|^2\Gamma\left(\frac{3}{2} + 2S\right) + \sqrt{\pi}\Gamma(2 + 2S)\left(\frac{1}{2} + S\right)}{\sqrt{\pi}\Gamma(2 + 2S)}. \tag{26}$$

Equation (25) with  $\sigma^2$  substituted by expression (26) provides the NPSE for the vortex modes. In the case of  $S = 0$ , it carries over into NPSE derived for the modes with the transverse ground-state structure in Ref. [61].

### 3 Validation of results: numerical simulations

Results presented below were obtained by means of imaginary- and real-time simulations of the full GPE (8), and the use of the above approximations, *viz.*, *yrast* solution (13), TF solution (16) and 1D NPSE (25). The simulations were performed by dint of the split-step method based on the Crank–Nicolson algorithm [66]. The space and time steps employed in the numerical simulations are 0.04 and 0.001, respectively. The imaginary-time simulations produce lowest energy profiles, while real-time simulations make it possible to test their stability and dynamics. Below, we check the accuracy of 1D NPSE (25) by comparing axial density profiles, produced by it,  $\rho(z) = |f|^2$ , with their counterparts produced by full GPE (8) as

$$\rho(z) = 2\pi \int_0^\infty |\phi|^2 r dr, \tag{27}$$

as well as the axial profiles presented by the 3D approximations (13) and (16), obtained, respectively, by

$$\rho(z) = 2\pi \int_0^\infty u^2 r dr \tag{28}$$

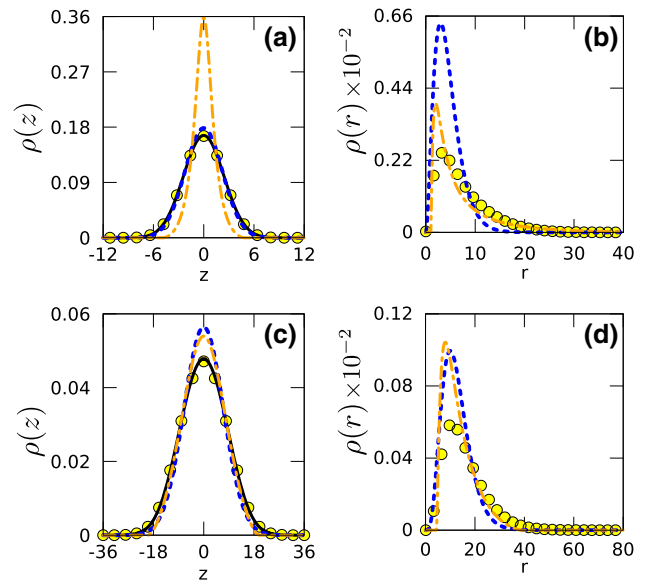


**Fig. 1** Normalized axial and radial density profiles for the vortex states ( $S = 1, 2$ ) in the self-repulsive BEC, under the action of the axial trapping potential (10). The radial profiles are calculated as per Eq. (30). The results produced by the full GPE (12), 1D NPSE (25), exact linear *yrast* solution (13), and TF approximation (16) are shown, respectively, by yellow circles, black solid lines, blue dashed lines and orange dot-dashed lines. Parameters used in the top panels are  $S = 1$ ,  $\lambda = 0.1$ , and  $g = 30$ , while those used in the bottom panel are  $S = 2$ ,  $\lambda = 0.01$ , and  $g = 80$ . The chemical potentials produced by means of the different methods in (a,b) are  $\mu_{\text{GPE}} = 2.85 \times 10^{-2}$ ,  $\mu_{\text{NPSE}} = 2.99 \times 10^{-2}$ ,  $\mu_{\text{yrast}} = -0.55 \times 10^{-2}$  and  $\mu_{\text{TF}} = -0.94 \times 10^{-2}$ ; and in (c,d)  $\mu_{\text{GPE}} = -7.95 \times 10^{-3}$ ,  $\mu_{\text{NPSE}} = -7.45 \times 10^{-2}$ ,  $\mu_{\text{yrast}} = -15 \times 10^{-3}$  and  $\mu_{\text{TF}} = -11.48 \times 10^{-3}$

and

$$\rho(z) = 2\pi \int_0^\infty u_{\text{TF}}^2 r dr. \tag{29}$$

In addition to the 1D density profiles produced by Eq. (25), it is possible to compare radial profiles,

$$\rho(r) = \int_{-\infty}^{+\infty} u^2 dz, \tag{30}$$

obtained from the full GPE (8), to their counterparts produced by the 3D approximations (13) and (16). The comparison is displayed in Fig. 1(b, d).

#### 3.1 Stationary ground and vortex states

We start the analysis by addressing the self-repulsive regime,  $g > 0$ , where localized states are supported by the weak axial potential (10). Figure 1a, b shows the normalized axial and radial density profile, respectively, for the radial vortex state with  $S = 1$  in the self-repulsive BEC, under the action of the axial trapping

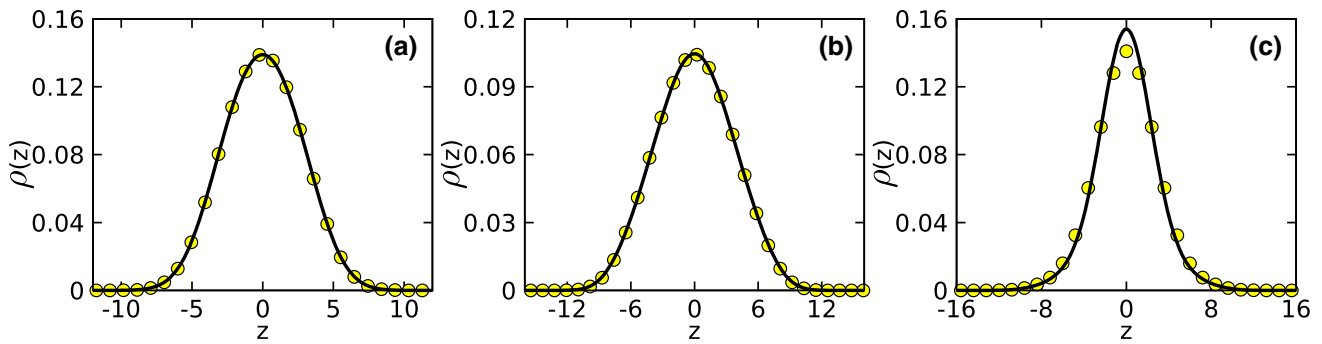


**Fig. 2** Normalized axial density profile  $\rho(z)$  for the ground state ( $S = 0$ ) in the self-repulsive BEC with nonlinearity strength  $g = 1$  (a),  $g = 10$  (b), and  $g = 100$  (c), in the presence of axial potential (10) with  $\lambda = 0.1$ . The density profiles

obtained by the numerical solution of the full GPE (12) and its 1D NPSE counterpart (25) are displayed, respectively, by yellow circles and black solid lines

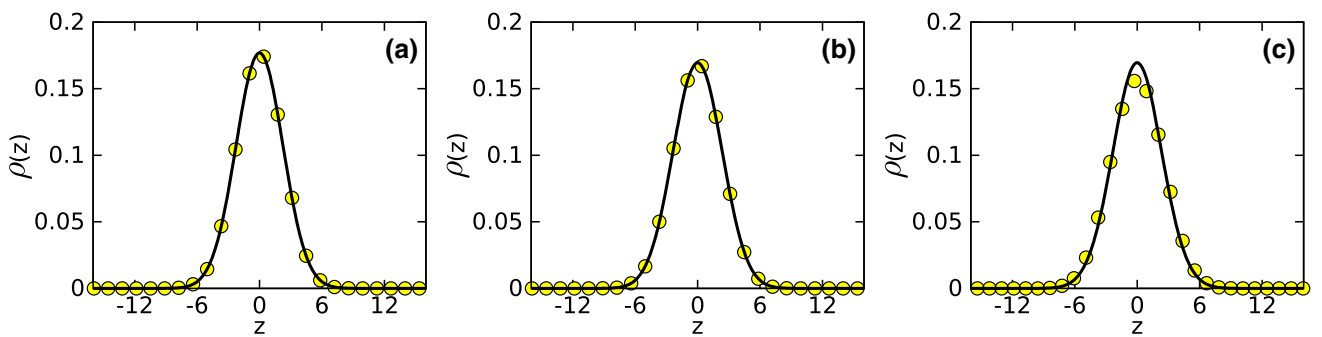


**Fig. 3** The same as in Fig. 2, but for vortex states with  $S = 1$

potential (10). It is seen that the solutions produced by the 1D NPSE present axial densities which are indistinguishable from those produced by the full GPE, while the other approximations are not adequate. Unlike the axial structure, the radial density provided by the 3D approximations does not produce accurate results when compared to the full GPE. In particular, although the *yrast* solution (13) produces an appropriate approximate result for the axial density, the same is not true as concerns the radial direction.

In Fig. 1c–d, we present normalized axial and radial density profiles, similar to those in Fig. 1a, b, but for the radial vortex state with  $S = 2$ . Again, we observe that the 1D NPSE produces accurate results, in comparison to those provided by the full GPE. In addition, the chemical potential of the 1D NPSE  $\mu_{\text{NPSE}}$  also presents the best result when comparing with the other approximations. On the other hand, analyzing the radial density, we conclude that both approximations produce a discrepancy in comparison to results obtained from the numerical solutions of the full GPE. Thus, for these configurations only 1D NPSE produces accurate results.

On the basis of the findings presented in Fig. 1, where only 1D NPSE accurately predicts the full GPE results, below we focus solely on the 1D NPSE—full GPE comparison. As a reference, in Fig. 2, we display the ground-state profiles ( $S = 0$ ) for three different values of strength  $g$  of the repulsive nonlinearity. Actually, these results were originally produced in Ref. [61], and are included here for the sake of the comparison. Next,

in Fig. 3, we present new results for the vortex modes with  $S = 1$  and the same values of  $g$ . The figure definitely corroborates that the effective 1D NPSE (25) produces very accurate results in comparison to those obtained from the full GPE (8).

To extend the consideration of the self-repulsive nonlinearity, in Fig. 4a, we present the axial density profiles for BEC with  $g = 10$ , trapped in the axial potential (10), with different vorticities. It is worthy to note a conspicuous difference in the density profiles between the ground states and the vortex with  $S = 1$ , while differences between the profiles pertaining to  $S = 1, 2$ , and 3 are very small. To quantify this feature, we define the relative difference of peak values of the density, at  $z = 0$ :

$$\delta\rho(S, S + 1) = |\rho_{\text{max}}(S) - \rho_{\text{max}}(S + 1)|/\rho_{\text{max}}(S). \tag{31}$$

The numerical data produced by the solution of Eqs. (25) and (26), substituted in Eq. (31), yield the following values:  $\delta\rho(0, 1) = 0.62$ ,  $\delta\rho(1, 2) = 0.03$ , and  $\delta\rho(2, 3) = 0.007$ . Further, Fig. 4b demonstrates very similar results obtained for the same settings from the full GPE. In Fig. 4c, the findings produced by the 3D  $\rightarrow$  1D reduction are additionally represented by axial profiles of the transverse width,  $\sigma$ , see Eq. (26).

Similar to the case of the repulsion, for the attractive sign of the nonlinearity ( $g < 0$ ) the 1D NPSE (25) also provides accurate results in comparison to the underlying



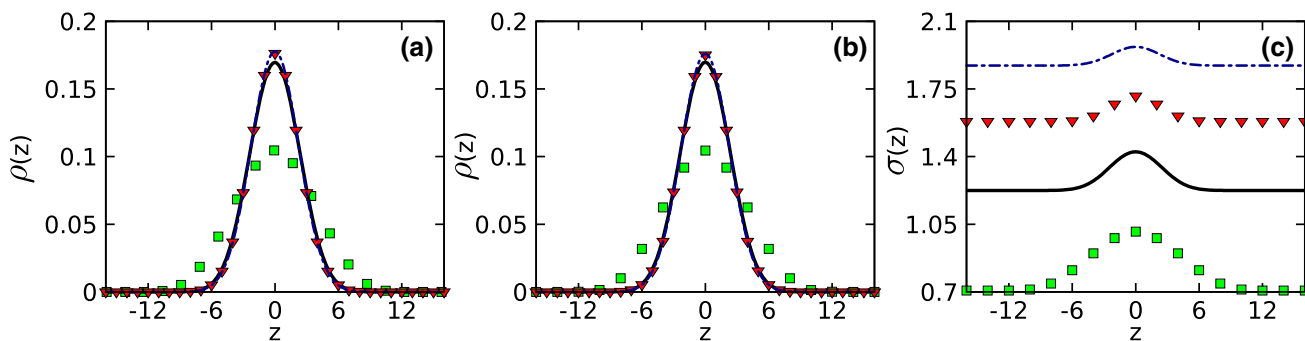


**Fig. 4** **a** Normalized axial density profiles  $\rho(z)$  for the repulsive condensate with  $g = 10$ , under the action of the axial external potential (10) with  $\lambda = 0.1$ , produced by the numerical solution of the 1D NPSE, for different values of the vorticity:  $S = 0, 1, 2$ , and  $3$ , are plotted by green squares, black solid lines, red triangles, and blue dashed lines, respec-

tively. **b** The same as in **a**, but produced by the full GPE, displayed for the comparison. **c** Transverse width  $\sigma$ , as produced by Eq. (26), in the same setting as in **(a)**, is presented by the green squares for  $S = 0$ , black solid lines for  $S = 1$ , red triangles for  $S = 2$ , and blue dashed lines for  $S = 3$

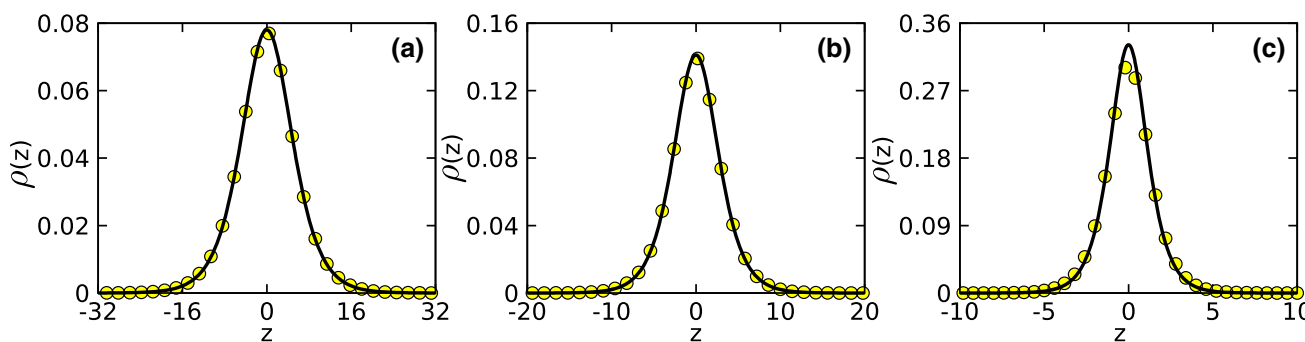


**Fig. 5** Normalized axial density profile  $\rho(z)$  for the ground state ( $S = 0$ ) in the self-attractive BEC with nonlinearity strength  $g = -0.3$  **(a)**,  $g = -0.5$  **(b)**, and  $g = -0.8$  **(c)**, in the absence of the axial potential ( $V(z) = 0$ ). The den-

sity profiles produced by the numerical solution of the full GPE (12) and its 1D NPSE counterpart (25) are displayed, respectively, by yellow circles and black solid lines

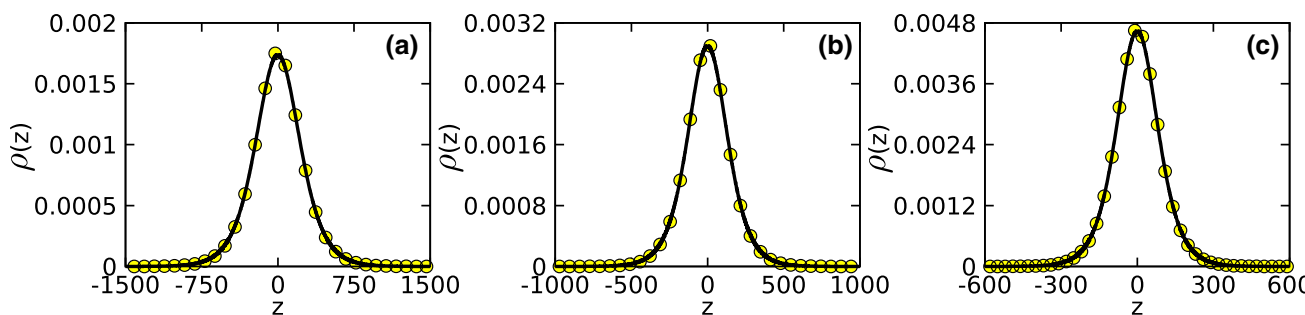


**Fig. 6** The same as in Fig. 5, but for the vortex states with  $S = 1$

ing GPE (8). As a reference for this case, in Fig. 5, we display the axial densities for the ground state ( $S = 0$ ), in the absence of the axial potential. Next, in Fig. 6, we display typical axial profiles for the same parameters, with vorticity  $S = 1$ . Again, the results obtained from the 1D NPSE are seen to be very accurate when compared to their counterparts produced by the full GPE. Thus, the 1D NPSE is equally accurate in reproducing the ground and vortex states of the GPE for both attractive and repulsive signs of the cubic nonlinearity in the 3D equation.

It is relevant to stress the great difference between the states with  $S = 0$  and  $1$  in the case of the self-attractive nonlinearity,  $g < 0$ : as is clearly seen from the comparison of Figs. 5 and 6, for the same norm, fixed as per Eq. (2), the vortex modes are much broader than their zero-vorticity counterparts, with a much smaller amplitude. On the other hand, the comparison of Figs. 2 and 3 demonstrates that there is little difference between the widths and amplitudes of the modes with  $S = 0$  and  $1$  in the case of the self-repulsion ( $g > 0$ ). This feature is easily explained by the fact that, in the case of  $g > 0$ , the width of the confined mode is chiefly deter-

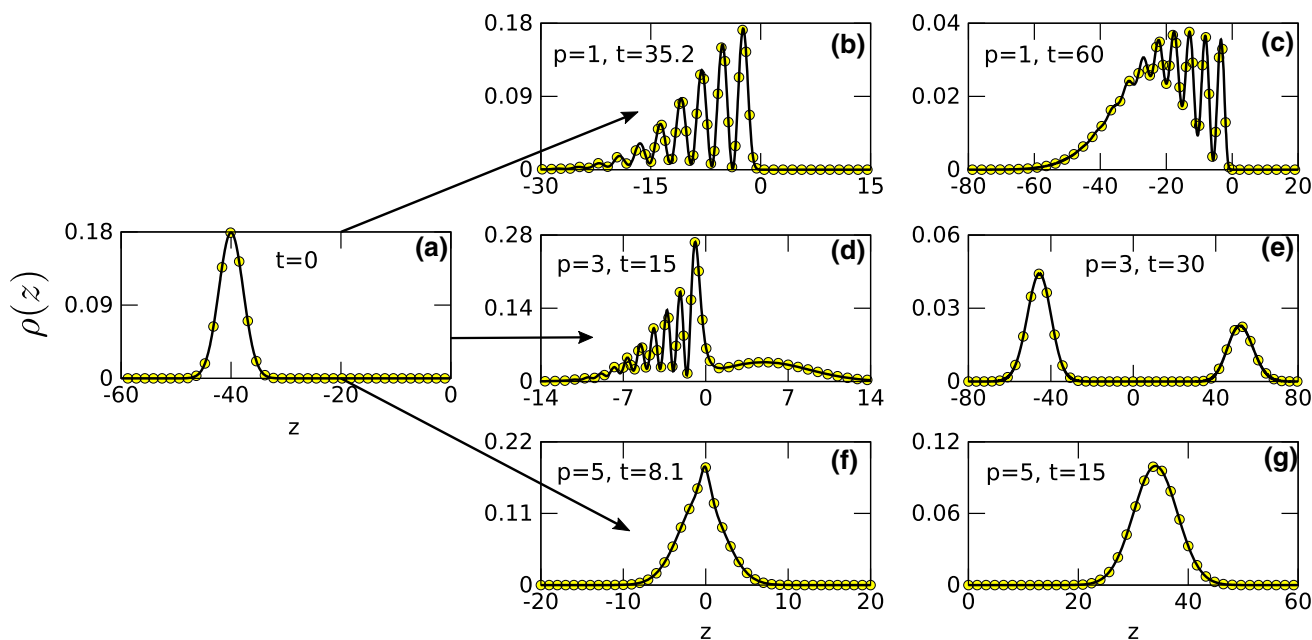


**Fig. 7** The evolution of the axial density profile for the quasi-soliton in the attractive BEC ( $g = -0.5$ ), with vorticity  $S = 1$ , which was set in motion by kick  $p = 1, 3$ , and  $5$  (see Eqs. (32) and (33)), in panels (b, c), (d, e) and (f, g), respectively, scattered by Gaussian barrier (34) with  $V_0 = 5$ . Panel (a) shows the initial axial density (at  $t = 0$ ), while

the middle (b,d,f) and right (c,e,g) panels display the axial densities during and after the collision with the scatterer, respectively. The profiles were produced by simulations of 1D NPSE (25) (black lines), and of full GPE (8) (yellow circles)

mined by the trapping potential, rather than by the intrinsic nonlinearity.

### 3.2 Collisions of fundamental and vortical modes with a potential barrier

Next, we address the accuracy of the 1D NPSE in dynamical settings. As a characteristic example, we consider scattering of an incident wave packet on an axial potential barrier. To this end, the initial conditions for the numerical simulations are taken as a stationary state, with different vorticities  $S$ , set in motion (boosted) by the kick factor with momentum  $p$ ,

$$\phi(r, z) \rightarrow \phi(r, z) \exp(ipz), \tag{32}$$

for the full GPE, and

$$f(z) \rightarrow f(z) \exp(ipz) \tag{33}$$

for the 1D NPSE. A scatterer which is commonly used in the experiment may be approximated by the Gaussian potential,

$$V_{\text{barrier}}(z) = V_0 \exp(-z^2), \tag{34}$$

with  $V_0 > 0$  [67].

In Fig. 7, we display the evolution of the axial density of a self-attractive BEC (with  $g = -0.5$ ) in the course of the collision between the incident wave packet and

barrier. To this end, we produce a vortex quasi-soliton, using both the 1D NLSE and full GPE, in the self-attractive model with  $g = -0.5$  under the action of trapping potential (10). The vortex quasi-soliton was set in motion by kicks with magnitude  $p = 1, 3$  and  $5$ . Then, it hits the Gaussian barrier (34) with  $V_0 = 5$ , exhibiting full reflection, splitting, or full transmission, respectively. Figure 7a shows the initial vortex state (at  $t = 0$ ) with  $S = 1$ . First, in Fig. 7b, c, the slowly moving vortex quasi-soliton, set in motion by kick  $p = 1$ , demonstrates total rebound of the wave packet with a deformed shape. Next, in Fig. 7d, e, the faster incident quasi-soliton, initially kicked by  $p = 3$ , splits in a larger bouncing fragment and a smaller transmitted one. Finally, in Fig. 7f, g, a fast quasi-soliton, kicked by  $p = 5$ , passes the barrier in an unscathed form. In all cases of the rebound, splitting, and passage, the simulations demonstrate, once again, that the results produced by the 1D NPSE are very close to their counterparts obtained from the simulations of the full 3D equation. In addition, it was observed that, after the collision with the barrier, in the case of the full reflection (Fig. 7b, c), the absolute value of the speed of the reflected solution is very close to the original one ( $p = 1$ ). For the case of  $p = 3$ , after the collision process, we observe two peaks with slightly different and opposite velocities ( $v_{\text{reflected}} \simeq -2.91$ ,  $v_{\text{transmitted}} \simeq 3.14$ ). Finally, for faster moving modes—for instance, with  $p = 5$ —the speed remains constant, except during the short time of the interaction with the barrier, when the speed drops by 8%. We stress that the vorticity fea-

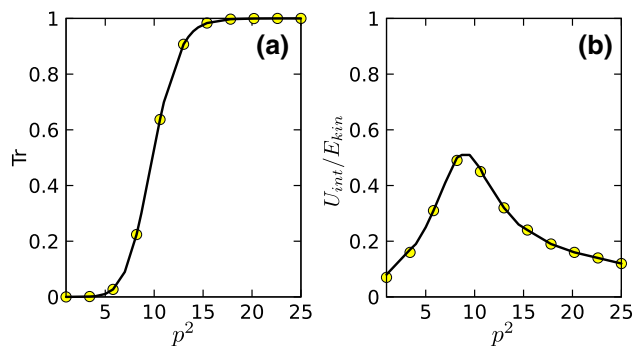


**Fig. 8** **a** The transmission coefficient for quasi-solitons in the attractive BEC, with  $g = -0.3$  and  $S = 1$ , colliding with scatterer (34) ( $V_0 = 5$ ), computed after the collision as per Eqs. (35) and (36). The results produced by the full GPE and 1D NPSE are shown by yellow circles and black lines, respectively. **b** The ratio  $U_{\text{int}}/E_{\text{kin}}$  obtained with the same parameters as in (a). Ratios  $U_{\text{int}}^{(3D)}/E_{\text{kin}}^{(3D)}$  and  $U_{\text{int}}^{(1D)}/E_{\text{kin}}^{(1D)}$  are displayed by yellow circles and black solid lines, respectively

ture in the radial structure (examples shown in Fig. 7) remains unchanged after the collision.

Findings produced by the simulations of the collisions of quasi-solitons carrying different velocities (introduced by  $p$ ) with the barrier are summarized in Fig. 8, which shows the transmission coefficient, defined as

$$\text{Tr}^{(3D)} \equiv 2\pi \int_0^\infty dz \int_0^\infty r|\phi|^2 dr \tag{35}$$

for the full GPE, and

$$\text{Tr}^{(1D)} \equiv \int_0^\infty |f|^2 dz \tag{36}$$

for the 1D NPSE, computed after completion of the collision. The dependence of the transmission coefficient on the kick parameter  $p^2$  (see Eqs. (32) and (33)) is displayed in Fig. 8a for  $S = 1$ . These results naturally demonstrate a transition from the full rebound ( $\text{Tr} = 0$ ) to complete transmission ( $\text{Tr} = 1$ ) with the increase of  $p^2$ . The virtual identity of the results produced by the 1D NPSE and GPE is evident in the entire range of the variation of  $p^2$ .

The collision of the incident wave packet with the scatterer (barrier) is characterized by comparison of the potential energy of the interaction with the barrier,  $U_{\text{int}}$ , and kinetic energy of the moving packet,  $E_{\text{kin}}$ . In the framework of the full GPE, these are

$$U_{\text{int}}^{(3D)} = 2\pi \int_{-\infty}^{+\infty} V_{\text{barrier}} dz \int_0^\infty |\phi|^2 r dr, \tag{37}$$

$$E_{\text{kin}}^{(3D)} = \pi \int_{-\infty}^{+\infty} \int_0^\infty \left( \left| \frac{\partial \phi}{\partial r} \right|^2 + \left| \frac{\partial \phi}{\partial z} \right|^2 \right) r dr dz, \tag{38}$$

see Eq. (6), and for the 1D NPSE the energies are identified as

$$U_{\text{int}}^{(1D)} = \int_{-\infty}^{+\infty} V_{\text{barrier}} |f|^2 dz, \tag{39}$$

$$E_{\text{kin}}^{(1D)} = \int_{-\infty}^{+\infty} \frac{1}{2} \left| \frac{\partial f}{\partial z} \right|^2 dz. \tag{40}$$

Accordingly, we calculate ratio  $U_{\text{int}}/E_{\text{kin}}$  for the vortex quasi-soliton with  $S = 1$  in the course of the evolution. The results, presented in Fig. 8b, show the maximum value of this ratio, which is, in most cases, reached at the moment when the incident wave packet is passing the barrier’s apex. Further, we observe the peak of  $U_{\text{int}}/E_{\text{kin}}$  when the setup features splitting with  $\text{Tr} \approx 44.2\%$ . Thus, the 1D NPSE again shows remarkably accurate results, in comparison to those produced by the full 3D GPE—this time, for the analysis of the scattering of the incident wave packet on the axial potential barrier.

Finally, we investigate the effect of the vorticity on the collision of the wave packet of the self-repulsive BEC ( $g = 10$ ), which was formed, as outlined above, in trapping potential (10), and then set in motion by kick  $p$ . Figure 9a–c displays the results for the ground state ( $S = 0$ ), which is set in motion at  $t = 0$  by the kick with  $p = 3.5$ , and collides with barrier (34) at  $t = 14$ . The results are displayed at  $t = 30$ . For the vortex state with  $S = 1$ , the results produced for the same parameters are different, as observed in Fig. 9d–f. Once again, in all the cases shown in Fig. 9, the results produced by the 1D NPSE are virtually identical to their counterparts obtained from the simulations of the full GPE.

### 3.3 Head-on collisions between solitons

Using solutions for localized modes propagating at opposite velocities makes it possible to simulate collisions between them. It is known that collisions between solitons at low velocities often lead to inelastic outcomes, while faster solitons pass through each other quasi-elastically [67–69]. In this context, we simulated collisions of the vortex and ground-state modes (actually, 1D solitons) in the self-attractive BEC, in the framework of the effective 1D NPSE (25), starting with the stationary profiles produced by this equation with  $V(z) = 0$ . Initially, they were created with centered placed at  $z = \mp z_0$ , and boosted as per Eq. (33). To preclude artifacts produced by interaction of the localized modes with radiation waves reflected from edges of the integration domain, absorbing boundary conditions were implemented at the edges, which broke the conservation of the 1D norm  $N_{1D} = \int_{-\infty}^{+\infty} |f(z, t)|^2 dz$ . In accordance with the normalization adopted above, the initial total norm of the two modes is  $N_{1D} = 2$ .

In Fig. 10a–d, we present two examples of elastic collisions. In Fig. 10a, the collision is fully elastic between fast solitons with  $S = 0$ , set in motion by strong kicks,



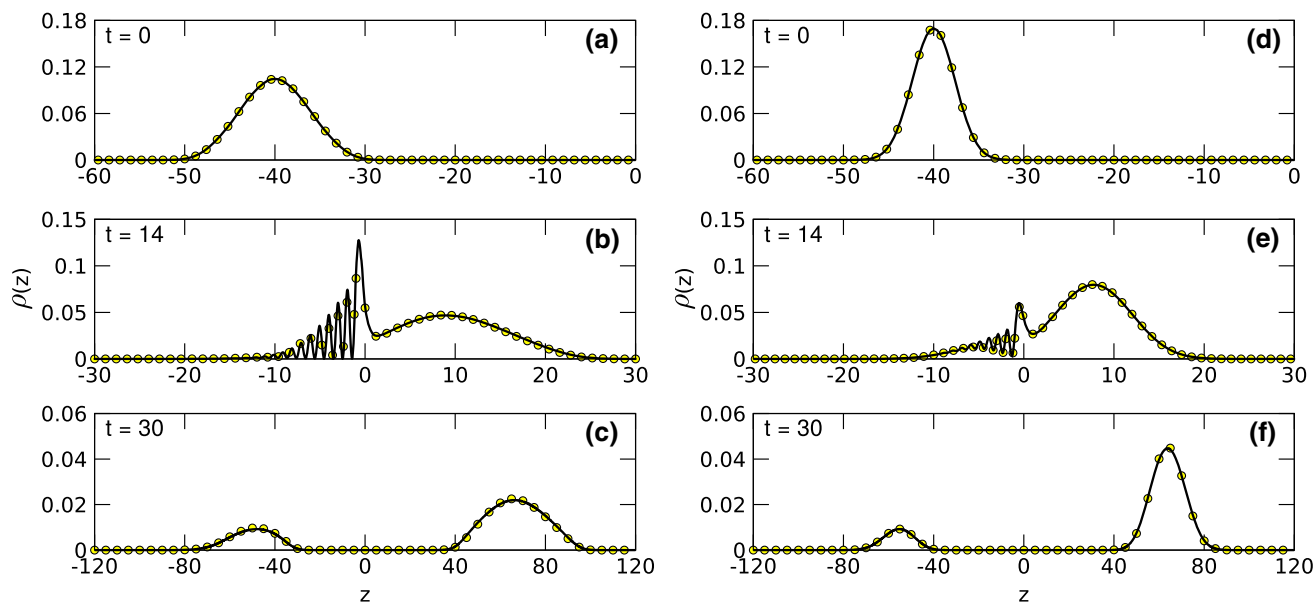


**Fig. 9** The evolution of the axial density profile in the repulsive BEC ( $g = 10$ ), formed as the ground state by trapping potential (10) with  $\lambda = 0.1$ , and set in motion by kick (32) or (33) with  $p = 3.5$ . The wave packet collides with

scatterer (34) that has  $V_0 = 5$ . Panels (a)–(c) and (d)–(f) display the findings for  $S = 0$  and  $S = 1$ , respectively. The results produced by the 1D NPSE and full GPE are shown, severally, by black solid lines and yellow circles

$p = \pm 15$ , in the case of  $g = -0.3$ . This collision does not change the value of the total norm. The fully elastic character of the collision is confirmed by Fig. 10b, which compares profiles  $|f(z, t = 0)|^2$  and  $|f(z, t = 15)|^2$ , exhibiting no difference between them.

In Fig. 10c, d, the elastic collision is plotted for the 1D solitons with  $S = 1$ , boosted by very small momenta  $p = \pm 0.005$  at  $g = -0.8$ . The simulations demonstrate that the range of the quasi-elasticity is much broader for  $S = 1$ , in comparison to  $S = 0$ , extending to extremely low values of  $|p|$ . This conclusion is naturally explained by the above-mentioned property of the solitons with  $S = 1$ , whose amplitude is much smaller than that of their counterparts with  $S = 0$ , cf. Figs. 5 and 6. As a consequence of the great difference in the amplitudes, the nonlinear interaction between the solitons and ensuing inelastic effects is much weaker in the case of  $S = 1$ .

Inelastic collisions between the solitons with  $S = 0$ , set in motion by weak kicks, are displayed in Fig. 11. Panels (a) and (b) present results of the simulations for  $g = -0.3$  and  $p = 0.01$ . It is seen that multiple (four) collisions take place in this case. Eventually, the quasi-solitons separate, at  $t > 6 \times 10^3$ . Figure 11b demonstrates that the colliding modes feature symmetry breaking, emerging with slightly different velocities. This effect is possible due to a mismatch between the “amplitude center” and “phase center” of the colliding soliton pair [70]. In this case, a small loss of the total norm occurs, from  $N_{1D} = 2$  at  $t = 0$  to  $N_{1D} = 1.99$  at  $t = 15 \times 10^3$ .

Another outcome of inelastic collisions between slowly moving 1D solitons corresponding to  $S = 0$  is their destruction. An example is presented in Fig. 11c, d, for

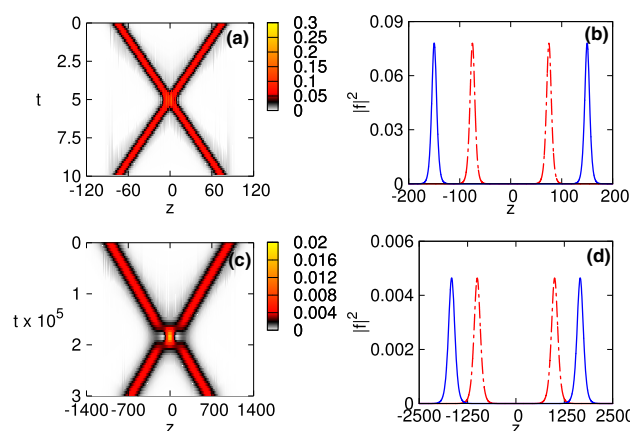


**Fig. 10** Left panels display head-on elastic collision between 1D solitons boosted by opposite kicks, as produced by simulations of the 1D equation (25) with  $g < 0$  (the self-attractive nonlinearity) and  $V(z) = 0$ . **a**  $g = -0.3$ ,  $p = \pm 15$  and  $S = 0$ , **(c)**  $g = -0.8$ ,  $p = \pm 0.005$  and  $S = 1$ . Panels **(b)** and **(d)** show the comparison between the initial profiles and the post-collision ones, corresponding to **(a)** and **(c)**, respectively. The initial profiles of  $|f(z, t = 0)|^2$  are shown by red dotted-dashed lines, while final ones, *viz.*,  $|f(z, t = 15)|^2$  in **(b)** and  $|f(z, t = 5 \times 10^5)|^2$  in **(d)**, are shown by blue solid lines

$g = -0.5$  and kicks  $p = \pm 0.1$ . As a result, at  $t = 750$ , the total norm drops from  $N_{1D} = 2$  to 0.74.

We also analyzed collisions between the 1D solitons corresponding to  $S = 1$  at extremely small values of the kick. In Fig. 12a, we present an example of an inelastic collision, obtained from the simulations of Eq. (25) with  $g = -1.5$ , for  $p = \pm 0.0001$ . In this case, a double col-

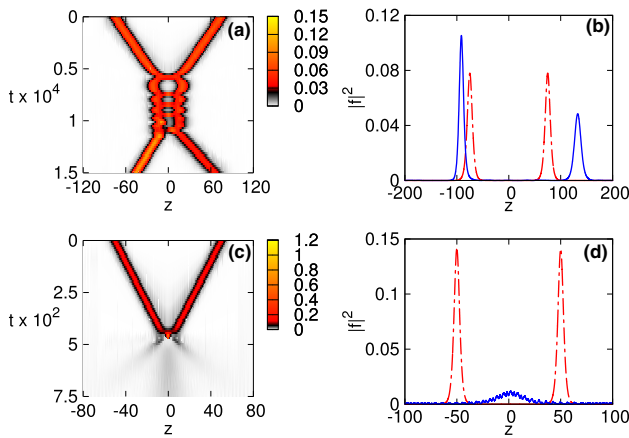


**Fig. 11** Left panels display inelastic collision between 1D solitons corresponding to  $S = 0$ , boosted by opposite momenta, as produced by simulations of Eq. (25) with  $V(z) = 0$ . **a**  $g = -0.3$  and  $p = \pm 0.01$ ; **(c)**  $g = -0.5$  and  $p = \pm 0.1$ . Panels **(b)** and **(d)** show the comparison between the initial and post-collision profiles corresponding to **(a)** and **(c)**, respectively. The initial profiles of  $|f(z, t = 0)|^2$  are shown by red dotted-dashed lines, while the final ones, *viz.*,  $|f(z, t = 2 \times 10^4)|^2$  in **(b)** and  $|f(z, t = 10^3)|^2$  in **(d)**, are shown by blue solid lines

lision takes place, leading to the symmetry breaking in the pair of eventually separating solitons, see Fig. 12b. In this case, the change of total 1D norm is negligible: from  $N_{1D} = 2$  at  $t = 0$  to 1.99 at  $t = 4.5 \times 10^6$ .

In the case of strong self-attraction, collisions between 1D solitons corresponding to  $S = 1$  lead to their complete destruction (similar to what is shown in Fig. 11c, d for the solitons corresponding to  $S = 0$ ) even at larger values of the kick. An example is displayed in Fig. 12c, d, for  $g = -10$  and  $p = \pm 0.5$ . The loss caused by the edge absorbers leads to the drop of the total norm from  $N_{1D} = 2$  at  $t = 0$  to  $N_{1D} = 1.35$  at  $t = 220$ .

The results of systematic simulations of the collisions are summarized, separately for the solitons with  $S = 0$  and 1, in Fig. 13a, b, respectively. The plots show borders between elastic and inelastic collisions (E.C. and I.C.),  $p_{crit}(g)$ , in the plane of  $(g, p^2)$ , the collisions being elastic at  $p^2 > p_{crit}^2(g)$ . The range displayed in the figure is restricted to  $0 > g > g_{crit} = -0.8$  for  $S = 0$  and  $g > g_{crit} = -12$  for  $S = 1$ . At  $g < g_{crit}$  the 1D Eq. (25) with  $g < 0$  admits the onset of the collapse, as well as the underlying 3D Eq. (8), cf. Ref. [28]. In all the cases, the change of  $g$  towards more negative values (larger  $|g|$ ) leads to stronger interactions and, consecutively, more inelastic outcomes of the collision. For example, the simulations of collisions between the solitons corresponding to  $S = 1$  demonstrate step enhancement of the inelasticity with the increase of  $|g|$ :  $p_{crit}(g = -0.3) = 0.036$ ,  $p_{crit}(g = -0.6) = 10.407$ ,  $p_{crit}(g = -0.7) = 5600$ . The same behavior is observed for the solitons with  $S = 1$ , with  $p_{crit}(g = -0.7) = 2 \times 10^{-7}$ ,  $p_{crit}(g = -1.5) = 5 \times 10^{-7}$ ,  $p_{crit}(g = -9) = 2.044$ . The simulations of collisions between the solitons corresponding to  $S = 2$  produce

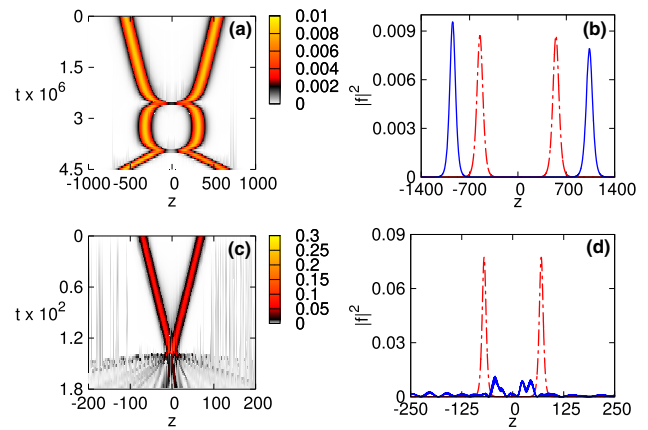


**Fig. 12** The same as in Figs. 10 and 11, but for the head-on collisions between 1D solitons corresponding to  $S = 1$ . **a**  $g = -1.5$  and  $p = \pm 0.0001$ ; **(c)**  $g = -10$  and  $p = \pm 0.5$ . In panels **(b)** and **(d)**, initial profiles of  $|f(z, t = 0)|^2$  are shown by red dotted-dashed lines (red), while the final profiles are shown by blue solid lines, *viz.*,  $|f(z, t = 5 \times 10^6)|^2$  in **(b)**, and  $|f(z, t = 220)|^2$  in **(d)**

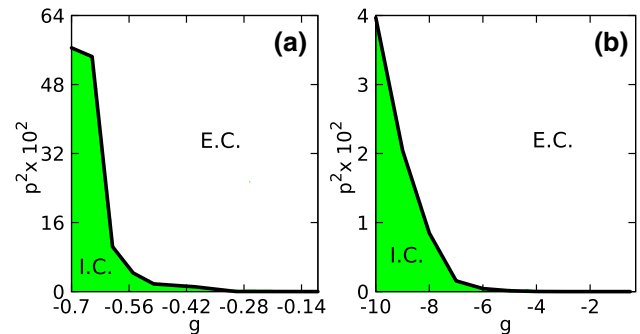


**Fig. 13** Diagrams of outcomes of collisions between 1D solitons, produced by simulations of Eq. (25) with  $S = 0$  **(a)** and  $S = 1$  **(b)**. Elastic and inelastic collisions (E.C. and I.C.) take place in the white and green areas, respectively

still much weaker inelastic effects (not shown here in detail).

### 3.4 Stability of vortex states in self-attractive BECs

The stability of stationary vortex states is an important issue, as it is well known that vortex solitons are typically subject to instability against spontaneous splitting, seeded by azimuthal perturbations [65]. To carry out the numerical analysis of this issue, we performed direct simulations of the evolution of vortices, slightly perturbed in the transverse plane, in the framework of 3D GPE (1) written in the Cartesian coordinates. The respective initial condition is

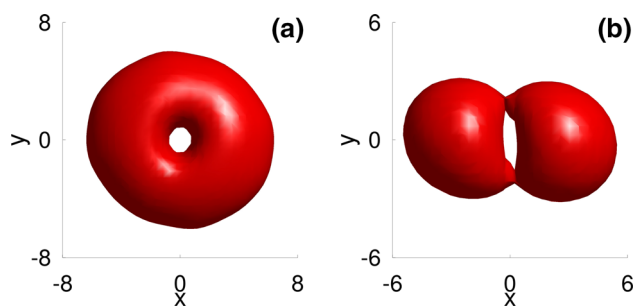


**Fig. 14** 3D density-isosurface snapshots for vortex states with  $S = 1$  in the self-attractive BEC, under the action of the axial external potential (10) with  $\lambda = 0.1$ . The results were produced by real-time simulations of 3D GPE (1), using initial condition (41), subject to normalization (42). **a** The isosurface profile with  $|\psi|^2 = 5 \times 10^{-4}$ , for  $g = -1.5$  at  $t = 6 \times 10^4$ . **b** The profile with  $|\psi|^2 = 9 \times 10^{-4}$  for  $g = -8.6$  at  $t = 165$

$$\psi(x, y, z; t = 0) = \mathcal{N}(x + iy)^S \times \exp\left(-\frac{1}{2}\sqrt{x^2 + \frac{y^2}{\alpha^2} - \frac{\lambda}{2}z^2}\right), \tag{41}$$

where constant  $\mathcal{N}$  is determined by the normalization condition

$$\int_{-\infty}^{+\infty} \int_{-\infty}^{+\infty} \int_{-\infty}^{+\infty} |\psi(x, y, z)|^2 dx dy dz = 1. \tag{42}$$

Parameter  $\alpha$  in Eq. (41) introduces asymmetry in the initial profile. For the simulations displayed here, we set  $\alpha = 1.1$ .

The numerical analysis reveals that the profiles with  $S = 1$  and  $g > -2$  show oscillations initiated by the asymmetric perturbation in input (41), but retain their structural integrity in the course of indefinitely long evolution. As an example, in Fig. 14a, we plot the 3D isosurface contour of the vortex state with  $S = 1$  and  $g = -1.5$  at  $t = 6 \times 10^4$ . Thus, we conclude that the vortex states with  $S = 1$  are stable against the transverse deformations at  $g \geq -2$ .

Taking stronger self-attraction with  $g < -2$ , we observe, as it may be expected, that the perturbed profiles abruptly lose their integrity, splitting into oscillating fragments, that later develop collapse (intrinsic blowup). A typical example is displayed in Fig. 14b for the vortex with  $S = 1$  and  $g = -8.6$ , where two fragments are almost completely separated at  $t = 165$  (shortly before the onset of the intrinsic collapse). This analysis is reported in Fig. 14 for  $\lambda = 0.1$ , i.e., in the presence of the trapping potential (10). The consideration of the stability of the vortex solitons in the absence of the trap is a numerically challenging problem, as the solitons' tails tend to be strongly extended in this case.

We have also addressed the (in)stability of vortices with  $S = 2$  and 3. Unlike the case of  $S = 1$ , no stable profile was found. For ones with  $S = 2$ , the evolution

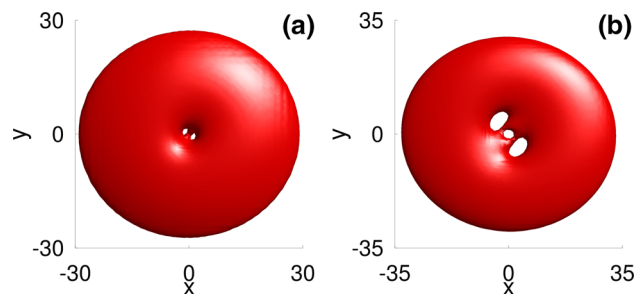


**Fig. 15** The same as in Fig. 14, but for vortices with  $S = 2$  and 3. **a** The isosurface profile with  $|\psi|^2 = 4 \times 10^{-6}$  for  $S = 2$  and  $g = -0.2$  at  $t = 40$ . **b** The profile with  $|\psi|^2 = 8 \times 10^{-6}$ , for  $S = 3$  and  $g = -0.1$  at  $t = 50$

of the input profile (41) leads to fission in two unitary vortices, which is also an instability scenario known in other models [65]. In particular, Fig. 15a shows the evolution of an unstable vortex with  $S = 2$  and  $g = -0.2$ . It is seen that, at  $t = 40$ , two unitary vortices, produced by the splitting instability from the double one, form a pair aligned in the radial direction. Similar results are produced by the simulations for the vortex with  $S = 3$ . In this case, the unstable evolution leads to the formation of three unitary vortices aligned along the diameter. The result is illustrated in Fig. 15b, which displays a snapshot of the 3D density profile of a triple vortex for  $g = -0.1$  at  $t = 50$ .

The results of the (in)stability reported here for the self-attractive BEC are in agreement with those previously reported for the 2D NPSE [42, 71] and cubic 2D NLSE [65, 72–74].

### 4 Conclusion

In this work, we have extended the recently developed analysis of the mean-field dynamics of BEC transversely confined by the 2D funnel-shaped potential (9), which is related to the class of nonlinear BEC models with singular potentials [75]. While previously it was elaborated for fundamental states, we have here presented it for vortex modes, starting from the 3D GPE, for both repulsive and attractive signs of the nonlinearity (in the former case, an axial trapping potential is necessarily included too). In the full 3D form, wave functions of the *yrast* eigenstates are found as exact solutions of the linearized GPE, and nonlinear states are found by means of the TF (Thomas–Fermi) approximation for the case of the self-repulsive nonlinearity. Further, using the variational approach, the effective 1D NPSE (nonpolynomial Schrödinger equation) has been derived for the tightly trapped modes, with zero and nonzero intrinsic vorticities in the transverse plane. Systematically collected numerical results corroborate high accuracy of the NPSE, in comparison with the full 3D GPE, in predicting shapes of the modes and results of their collisions with an axial potential scatterer. In addition to that, elastic and inelastic collisions between

1D solitons are studied in detail by means of simulations of NPSE with the attractive sign of the nonlinearity. Also identified is the critical value of the self-attraction strength which separates vortex states with winding number  $S = 1$  which are stable and unstable against splitting in two fragments, and it is demonstrated that all vortices with  $S = 2$  and 3 are unstable against the splitting.

It may be interesting to extend the analysis for BEC in the form of the above-mentioned quantum droplets, which are modeled by the GPE including additional terms which take into account higher order self-repulsion terms induced by quantum fluctuations around the mean-field states [18, 19, 24].

**Acknowledgements** The authors acknowledge financial support from the Brazilian agencies CNPq (#304073/2016-4 & #425718/2018-2), CAPES, and FAPEG (PRONEM #201710267000540 & PRONEX #201710267000503). This work was performed as part of the Brazilian National Institute of Science and Technology (INCT) for Quantum Information (#465469/2014-0). The work B.A.M. is supported, in part, by the Israel Science Foundation through Grant No. 1286/17.

**Data availability statement** This manuscript has no associated data or the data will not be deposited. [Authors' comment: No associated data is deposited, as it is not necessary for the presentation of the results in the paper.]

## References

1. F. Dalfovo, S. Giorgini, L.P. Pitaevskii, S. Stringari, *Rev. Mod. Phys.* **71**, 463 (1999)
2. L. P. Pitaevskii and S. Stringari, *Bose-Einstein Condensation*, International Series of Monographs on Physics (Clarendon Press, 2003)
3. C.J. Pethick, H. Smith, *Bose-Einstein Condensation in Dilute Gases* (Cambridge University Press, Cambridge, 2008)
4. M.H. Anderson, J.R. Ensher, M.R. Matthews, C.E. Wieman, E.A. Cornell, *Science* **269**, 198 (1995)
5. K.B. Davis, M.O. Mewes, M.R. Andrews, N.J. van Druten, D.S. Durfee, D.M. Kurn, W. Ketterle, *Phys. Rev. Lett.* **75**, 3969 (1995)
6. C.C. Bradley, C.A. Sackett, J.J. Tollett, R.G. Hulet, *Phys. Rev. Lett.* **75**, 1687 (1995)
7. S. Burger, K. Bongs, S. Dettmer, W. Ertmer, K. Sengstock, A. Sanpera, G.V. Shlyapnikov, M. Lewenstein, *Phys. Rev. Lett.* **83**, 5198 (1999)
8. L. Khaykovich, F. Schreck, G. Ferrari, T. Bourdel, J. Cubizolles, L.D. Carr, Y. Castin, C. Salomon, *Science* **296**, 1290 (2002)
9. K.E. Strecker, G.B. Partridge, A.G. Truscott, R.G. Hulet, *Nature* **417**, 150 (2002)
10. S.L. Cornish, S.T. Thompson, C.E. Wieman, *Phys. Rev. Lett.* **96**, 170401 (2006)
11. J. Denschlag, J. E. Simsarian, D. L. Feder, C. W. Clark, L. A. Collins, J. Cubizolles, L. Deng, E. W. Hagley, K. Helmer, W. P. Reinhardt, S. L. Rolston, B. I. Schneider, and W. D. Phillips, *Science* **287**, 97 (2000)
12. P. Meystre, *Atom Optics* (Springer, 2001)
13. A.D. Martin, J. Ruostekoski, *New J. Phys.* **14**, 043040 (2012)
14. G.D. McDonald, C.C.N. Kuhn, K.S. Hardman, S. Bennetts, P.J. Everitt, P.A. Altin, J.E. Debs, J.D. Close, N.P. Robins, *Phys. Rev. Lett.* **113**, 013002 (2014)
15. J.L. Helm, S.L. Cornish, S.A. Gardiner, *Phys. Rev. Lett.* **114**, 134101 (2015)
16. A. Di Carli, C.D. Colquhoun, G. Henderson, S. Flannigan, G.L. Oppo, A.J. Daley, S. Kuhr, E. Haller, *Phys. Rev. Lett.* **123**, 123602 (2019)
17. D. Luo, Y. Jin, J.H.V. Nguyen, B.A. Malomed, O.V. Marchukov, V.A. Yurovsky, V. Dunjko, M. Olshanii, R.G. Hulet, *Phys. Rev. Lett.* **125**, 183902 (2020)
18. D.S. Petrov, *Phys. Rev. Lett.* **115**, 155302 (2015)
19. D.S. Petrov, G.E. Astrakharchik, *Phys. Rev. Lett.* **117**, 100401 (2016)
20. C. Cabrera, L. Tanzi, J. Sanz, B. Naylor, P. Thomas, P. Cheiney, L. Tarruell, *Science* **359**, 301 (2018)
21. P. Cheiney, C.R. Cabrera, J. Sanz, B. Naylor, L. Tanzi, L. Tarruell, *Phys. Rev. Lett.* **120**, 135301 (2018)
22. G. Semeghini, G. Ferioli, L. Masi, C. Mazzi, L. Wolswijk, F. Minardi, M. Modugno, G. Modugno, M. Inguscio, M. Fattori, *Phys. Rev. Lett.* **120**, 235301 (2018)
23. C. D'Errico, A. Burchianti, M. Prevedelli, L. Salasnich, F. Ancilotto, M. Modugno, F. Minardi, C. Fort, *Phys. Rev. Res.* **1**, 033155 (2019)
24. Z.-H. Luo, W. Pang, B. Liu, Y.-Y. Li, B.A. Malomed, *Front. Phys.* **16**, 1 (2021)
25. F. Büttcher, J.-N. Schmidt, J. Hertkorn, K.S.H. Ng, S.D. Graham, M. Guo, T. Langen, T. Pfau, *Rep. Prog. Phys.* **84**, 012403 (2021)
26. A.D. Jackson, G.M. Kavoulakis, C.J. Pethick, *Phys. Rev. A* **58**, 2417 (1998)
27. M. Chiofalo, M. Tosi, *Phys. Lett. A* **268**, 406 (2000)
28. L. Salasnich, A. Parola, L. Reatto, *Phys. Rev. A* **65**, 043614 (2002)
29. P. Massignan, M. Modugno, *Phys. Rev. A* **67**, 023614 (2003)
30. A.M. Kamchatnov, V.S. Shchesnovich, *Phys. Rev. A* **70**, 023604 (2004)
31. W. Zhang, L. You, *Phys. Rev. A* **71**, 025603 (2005)
32. A. Maluckov, L. Hadzievski, B.A. Malomed, L. Salasnich, *Phys. Rev. A* **78**, 013616 (2008)
33. S.K. Adhikari, L. Salasnich, *Phys. Rev. A* **77**, 033618 (2008)
34. L. Salasnich, F. Toigo, *Phys. Rev. A* **78**, 053626 (2008)
35. S. Adhikari, *Laser Phys. Lett.* **6**, 901 (2009)
36. S.K. Adhikari, B.A. Malomed, *Physica D* **238**, 1402 (2009)
37. S.K. Adhikari, *J. Phys. B At. Mol. Opt. Phys.* **43**, 085304 (2010)
38. M. C. P. dos Santos and W. B. Cardoso, *Phys. Rev. E* **103**, 052210 (2021)
39. A. Muñoz Mateo and V. Delgado, *Phys. Rev. A* **77**, 013617 (2008)
40. G. Gligorić, A. Maluckov, L. Hadzievski, B.A. Malomed, *J. Phys. B At. Mol. Opt. Phys.* **42**, 145302 (2009)
41. G. Gligorić, A. Maluckov, L. Hadzievski, B.A. Malomed, *Phys. Rev. A* **79**, 053609 (2009)



42. L. Salasnich, B.A. Malomed, *Phys. Rev. A* **79**, 053620 (2009)
43. L. Salasnich, *J. Phys. A Math. Theor.* **42**, 335205 (2009)
44. Luis E. Young-S., L. Salasnich, and S. K. Adhikari, *Phys. Rev. A* **82**, 053601 (2010)
45. W.B. Cardoso, A.T. Avelar, D. Bazeia, *Phys. Rev. E* **83**, 036604 (2011)
46. L. Salasnich, B.A. Malomed, *J. Phys. B At. Mol. Opt. Phys.* **45**, 055302 (2012)
47. L. Salasnich and B. A. Malomed, *Phys. Rev. A - At. Mol. Opt. Phys.* **87**, 063625 (2013)
48. L. Salasnich, W.B. Cardoso, B.A. Malomed, *Phys. Rev. A* **90**, 033629 (2014)
49. M.C. dos Santos, W.B. Cardoso, *Phys. Lett. A* **383**, 1435 (2019)
50. C. Wang, P. Kevrekidis, T. Horikis, D. Frantzeskakis, *Phys. Lett. A* **374**, 3863 (2010)
51. A.I. Nicolin, M.C. Raportaru, *Phys. A Stat. Mech. its Appl.* **389**, 4663 (2010)
52. C.A.G. Buitrago, S.K. Adhikari, *J. Phys. B At. Mol. Opt. Phys.* **42**, 215306 (2009)
53. H.L.C. Couto, W.B. Cardoso, *J. Phys. B At. Mol. Opt. Phys.* **48**, 025301 (2015)
54. S. Middelkamp, G. Theocharis, P.G. Kevrekidis, D.J. Frantzeskakis, P. Schmelcher, *Phys. Rev. A* **81**, 053618 (2010)
55. G. Theocharis, A. Weller, J.P. Ronzheimer, C. Gross, M.K. Oberthaler, P.G. Kevrekidis, D.J. Frantzeskakis, *Phys. Rev. A* **81**, 063604 (2010)
56. A.M. Mateo, V. Delgado, B.A. Malomed, *Phys. Rev. A* **83**, 053610 (2011)
57. W.B. Cardoso, J. Zeng, A.T. Avelar, D. Bazeia, B.A. Malomed, *Phys. Rev. E* **88**, 025201 (2013)
58. A.M. Mateo, V. Delgado, *Phys. Rev. E* **88**, 042916 (2013)
59. T. Yang, A.J. Henning, K.A. Benedict, *J. Phys. B At. Mol. Opt. Phys.* **47**, 035302 (2014)
60. H.L.C. Couto, A.T. Avelar, W.B. Cardoso, *Ann. Phys.* **530**, 1700352 (2018)
61. M.C.P. dos Santos, B.A. Malomed, W.B. Cardoso, *J. Phys. B At. Mol. Opt. Phys.* **52**, 245301 (2019)
62. B. Mottelson, *Phys. Rev. Lett.* **83**, 2695 (1999)
63. G.F. Bertsch, T. Papenbrock, *Phys. Rev. Lett.* **83**, 5412 (1999)
64. A.L. Fetter, *Rev. Mod. Phys.* **81**, 647 (2009)
65. B.A. Malomed, *Physica D* **399**, 108 (2019)
66. P. Muruganandam, S.K. Adhikari, *Comput. Phys. Commun.* **180**, 1888 (2009)
67. J.H. Nguyen, P. Dyke, D. Luo, B.A. Malomed, R.G. Hulet, *Nature Physics* **10**, 918 (2014)
68. Y.S. Kivshar, B.A. Malomed, *Rev. Mod. Phys.* **61**, 763 (1989)
69. S. Gatz, J. Herrmann, *J. Opt. Soc. Am. B* **8**, 2296 (1991)
70. L. Khaykovich, B.A. Malomed, *Phys. Rev. A* **74**, 023607 (2006)
71. M.C.P. dos Santos, B.A. Malomed, W.B. Cardoso, *Phys. Rev. E* **102**, 042209 (2020)
72. D. Mihalache, D. Mazilu, B.A. Malomed, F. Lederer, *Phys. Rev. A* **73**, 043615 (2006)
73. T.J. Alexander, L. Bergé, *Phys. Rev. E* **65**, 026611 (2002)
74. H. Saito, M. Ueda, *Phys. Rev. Lett.* **89**, 190402 (2002)
75. E. Shamriz, Z. Chen, B. A. Malomed, and H. Sakaguchi, Singular mean-field states: a brief review of recent results. *Condensed Matter* **5**, 20 (2020)